

Engineering topological materials in microwave cavity arrays

Brandon M. Anderson, Ruichao Ma, Clai Owens, David I. Schuster, Jonathan Simon
James Franck Institute and University of Chicago

We present a scalable architecture for the exploration of interacting topological phases of photons in arrays of microwave cavities, using established techniques from cavity and circuit quantum electrodynamics. A time-reversal symmetry breaking (non-reciprocal) flux is induced by coupling the microwave cavities to ferrites, allowing for the production of a variety of topological band structures including the $\alpha = 1/4$ Hofstadter model. Effective photon-photon interactions are included by coupling the cavities to superconducting qubits, and are sufficient to produce a $\nu = 1/2$ bosonic Laughlin puddle. We demonstrate by exact diagonalization that this architecture is robust to experimentally achievable levels of disorder. These advances provide an exciting opportunity to employ the quantum circuit toolkit for the exploration of strongly interacting topological materials.

I. INTRODUCTION

Despite significant interest in topological physics, the experimental success in realizing *strongly correlated* topological systems has thus far been limited to the fractional-quantum hall (FQH) effect [1, 2] in two-dimensional electron gases. There has recently been significant theoretical explorations of alternative realizations of FQH systems (and related fractional Chern insulators [3, 4]) in the field of “quantum engineering.” Here a topologically nontrivial Hamiltonian is built from the ground up, typically following a two-ingredient recipe [3, 4]: (1) strong interactions are added to a (2) topologically non-trivial single particle band structure. This recipe is well motivated theoretically, and experimentally there has been success in individual implementation of each ingredient. For example, ultracold atomic systems have experimentally succeeded in the study of both topologically novel band structures [5–9], and strongly interacting but topologically trivial systems [10, 11]. However, the simultaneous implementation of both elements, as is necessary for creating strongly correlated topological states, has thus far remained elusive.

Photons are a newly emerging platform for quantum engineering. Photonic crystals have successfully simulated non-interacting band structures in the regime of RF [12], microwave [13], or optical [14, 15] domains. In all cases, the necessary addition of strong interactions to produce strongly correlated states has remained challenging. On the other hand, strong photon-photon interactions are readily achieved in circuit QED experiments where the exquisite control over few qubit states has allowed the quantum simulation of, e.g., molecular energies [16]. Superconducting circuits have also been advanced as a route to strongly correlated photonic lattices [17, 18]. Implementing a time-reversal-symmetry breaking (TRSB) single particle band structure is still necessary to advance towards FQH physics; current proposals require site-dependent parametric modulation [18, 19], which remains experimentally difficult to scale to larger system sizes. Breaking time reversal symmetry with passive circuit elements would therefore be a significant advance in engineering of synthetic quantum materials.

Here we propose a new photonic platform to engineer two-dimensional tight binding models with non-trivial band topology, using arrays of three-dimensional microwave cavities. Such cavities can be easily machined from metal to work in the few-to-tens of GHz regime, and have been shown to provide exceptional coherence at cryogenic temperatures with quality factors exceeding $Q > 10^8$ [20]. The cavities can be tunnel-coupled evanescently by, e.g., directly milling a channel between two cavities, or using capacitively coupled transmission lines. Modern machining techniques allow the creation of scalable lattices with low disorder in on-site energies and tunneling energies.

A key component of our scheme is a new technique used to induce the requisite TRSB flux: this flux is induced by the onsite mode structure [21] of the cavity, in contrast to previous schemes [12, 15, 17, 22] that induce a Peierl’s phase in the tunnel coupler. The complex amplitude of the tunnel coupler depends on the local electric field at the periphery of the cavity. A non-reciprocal (TRSB) phase will require an electric field with on-site angular momentum, which is coupled to the polarization of the magnetic field through Faraday’s law [23]. Therefore, by coupling the magnetic field to a magnetic dipole, say through use of a ferrimagnetic crystal with a biased magnetic field [24, 25], a cavity mode with definite angular momentum can be energetically isolated. In this way, the ferrite transfers the TRSB bias field to a TRSB flux of the photonic lattice. This technique is experimentally advantageous compared to previous schemes because: (1) It allows for the *passive* creation of topological band structures, and therefore avoids issues with non-linear mixing with pumping frequency in modulated tunnel couplings schemes [18, 19]. (2) The ferrite couples to a chiral “bright” mode, shifting it in energy, leaving an unshifted chiral “dark” mode. The frequency of the dark mode is first-order insensitive to both the ferrite coupling strength, loss, and detuning from cavity resonance [26]; it is thus ideal for engineering low-disorder time-reversal breaking lattice models.

The final ingredient necessary for the study of FQH-like physics is strong photon-photon interactions. These can be incorporated by coupling the microwave cavities

to superconducting qubits [17, 27]. We consider adding such qubits to each site of the square Hofstadter model constructed from the linear circuit elements. The Hamiltonian describing the effective model can be simulated using exact diagonalization techniques. We therefore numerically explore our system at finite size and for few photons. The numerical results demonstrate our architecture will have a FQH eigenstate corresponding to a bosonic $\nu = 1/2$ Laughlin state on a lattice [9, 28].

In remainder of this paper we present a scalable architecture for study of strongly correlated topological materials. The organization of the paper is as follows: In Sec. II we discuss the general structure of the microwave cavities needed for our architecture. We then introduce on-site coupling elements (Sec. II A) which isolate a desired eigenmode on each lattice site. When these eigenmodes are tunnel coupled (Sec. II B) an effective flux emerges when the system is probed in a certain frequency range. This effective flux can be understood as an emergent gauge field (Sec. II C) arising from band projection. Concluding the discussion of the general non-interacting circuit elements, we show this architecture is sufficient to simulate the Hofstadter model (Sec. II D), and present proposals for some other interesting lattice models (Sec. II E.) In Sec. III we then consider the effects of adding photon-photon interactions to each site for the purpose of producing fractional Chern insulating states in finite-size systems. We use a numerical exact diagonalization technique to simulate our system, and find that the properties of a $\nu = 1/2$ bosonic “Laughlin puddle” emerge. Finally, in Sec. III A we consider the likely forms of disorder in the effective tight-binding model description of our system. We find that the system is insensitive to the largest sources of disorder, whereas the most sensitive forms of disorder can be controlled. We conclude that current experimental techniques should be sufficient to simulate strongly correlated topological systems.

II. SINGLE-PARTICLE BUILDING BLOCKS

We now describe the single particle building blocks for our microwave architecture. Our goal is to engineer an effective tight-binding Hamiltonian, \mathcal{H}_{eff} , for photons whose energy is near $\hbar\omega_0$. We will use a unique cavity eigenmode at this characteristic energy to represent the tight-binding degree of freedom (and thus restrict our work to “spinless” models.) To model \mathcal{H}_{eff} we therefore need an isolated eigenmode on every site, whose frequency is ω_0 , with all other onsite eigenmodes far detuned energetically.

There is significant freedom in the cavity mode structure. We describe a particular implementation employing transverse magnetic (TM) modes of cylindrical cavities with non-zero transverse magnetic field ($B_x, B_y \neq 0, B_z = 0$) and longitudinal electric field ($E_x, E_y = 0, E_z \neq 0$). We first consider a fundamental cavity mode tuned to frequency ω_0 (annihilated by a_0).

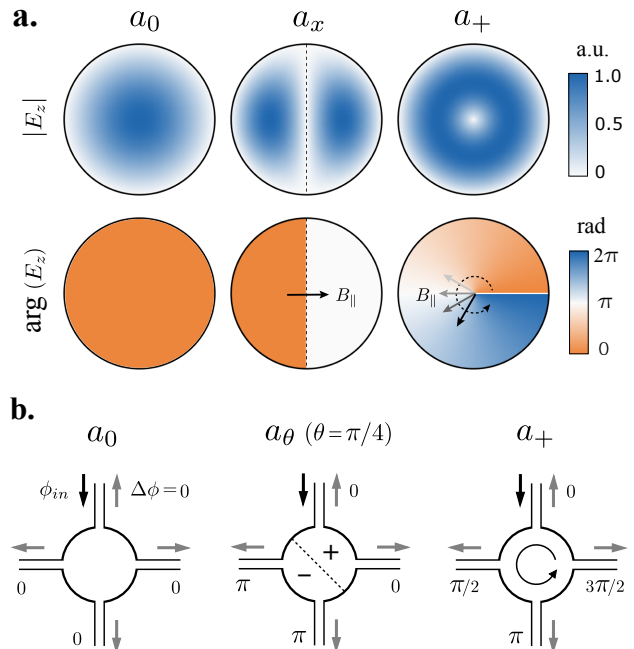


FIG. 1. (a) Structure of the electric field amplitude and phase (with corresponding magnetic field polarization) of the modes being considered. The fundamental mode has uniform phase everywhere with no nodes in the sole electric field component, E_z . The two-fold degenerate first excited manifold may be spanned by two modes with geometrically orthogonal linear-nodes in the E_z -field (a_x and a_y), or equivalently by two modes exhibiting a single point-node and $\pm 2\pi$ phase winding around the periphery (a_{\pm}). For the modes a_x and a_+ , the polarization of the magnetic field at the cavity center is presented. The polarization of the magnetic field points along the gradient of the phase of E_z . For linear modes the magnetic field is oriented perpendicular to the nodal line, with direction oscillating in time. For the chiral modes, this magnetic field polarization precesses in time with frequency ω_0 . The size of the circles does not reflect the physical dimension of the cavities, which is chosen such that the desired mode is always at frequency ω_0 . (b) The geometric phase acquired, for a photon of frequency ω_0 , when tunneling through a cavity in which each of type of mode has been isolated. (left) A fundamental mode cavity will induce no tunneling phase shift between any two contacts. (center) An isolated linear mode (via a diagonal conductor or dielectric) will induce a tunneling phase shift of either 0 or π . An isolated circular mode (via a ferrite in a magnetic field) will produce a phase shift equal to the relative angle between the incoming and outgoing tunnel-contacts.

The electric field of the fundamental mode, shown in Fig. 1(a), is nodeless and has a spatially uniform phase across the cavity. This is true regardless of the cavity geometry. We also consider a *different cavity* where the two-fold degenerate set of first excited modes (for example, TM_{210} , TM_{120} in a Cartesian basis[29]) is tuned to a frequency ω_0 . We define the annihilation operators of this manifold as $a_x(a_y)$, according to a node of the electric field along the $\hat{y}(\hat{x})$ -axis (see Fig.1(a)). Using this notation,

the onsite Hamiltonian is $\mathcal{H}^{(0)} = \omega_0 a_0^\dagger a_0$, for a fundamental mode cavity, and $\mathcal{H}^{(1)} = \omega_0 (a_x^\dagger a_x + a_y^\dagger a_y)$ for the excited cavity manifold. Here, and in what follows, we drop any constants resulting from zero point motion of the electromagnetic field, and set $\hbar = 1$.

While we have written the Hamiltonian in terms of \hat{x}/\hat{y} modes, this choice is arbitrary. Analogous to linearly polarized light, we may rotate the basis by an angle θ : $a_\theta = a_x \cos \theta + a_y \sin \theta$, and $a_{\theta+\pi/2} = -a_x \sin \theta + a_y \cos \theta$. Alternatively, we can construct a basis analogous to circularly polarized light: $a_\pm = (a_x \pm i a_y)/\sqrt{2}$, where the phase changes continuously by 2π going counter-clockwise (clockwise) around the cavity center in the a_+ (a_-) mode (see Fig. 1(a)). In this basis, the magnetic field has an amplitude maximum at the center of the cavity, and a polarization that lies in-plane and rotates uniformly in time at frequency ω_0 .

A. On-site symmetry breaking

The on-site degeneracy of $\mathcal{H}^{(1)}$ can be broken in a time-reversal preserving or time-reversal breaking manner. The first type takes the form of violations of cylindrical symmetry. For example, by placing a thin barrier (e.g. a rectangular conductor or dielectric) along the nodal line of the a_x mode, one adds a perturbation $\mathcal{V}^{(1)} = \Delta_{\text{lin}} a_y^\dagger a_y$ to the Hamiltonian $\mathcal{H}^{(1)}$. The a_x mode remains (nearly) unperturbed at frequency ω_0 , while the orthogonal a_y mode will be shifted to higher energy (by an amount Δ_{lin}). This energetically isolates the a_x mode at an energy ω_0 , and uniquely defines the relative phase between any two points on the edge of the cavity. (An analogous procedure isolates a_θ from $a_{\theta+\pi/2}$.) This perturbation only produces a relative phase of 0 or π between points on a cavity edge, and therefore cannot break time-reversal symmetry. Manufacturing imprecision gives rise to perturbations of this type.

For the study of quantum Hall physics, it is necessary to break time-reversal symmetry; this does not occur naturally for light. We consider achieving this by employing the coherent magnon interaction between cavity photons and the spins of a ferrimagnetic material [24, 25]: a small ferrite sphere placed at the center of the cavity with a DC bias field $\mathbf{B} = +B_0 \hat{z}$. The ferrite acts as a collective spin which couples to the magnetic field of the cavity mode and precesses at a frequency $\omega_F = \mu_0 B_0$. (If the bias field is reverse the following analysis is valid with $a_+ \leftrightarrow a_-$.) The magnetic field of the a_\pm modes has a maximum at the cavity center (at the node of the electric field), and an in-plane polarization that precesses about $\pm \hat{z}$ at a frequency ω_0 . When the spin precession frequency ω_F is tuned near ω_0 , the polarization of the magnetic field of the a_\pm mode rotates synchronously with the collective spin. The magnetic dipole interaction results in a strong coupling between the a_+ mode and the ferrite mode (denoted a_F). The magnetic field of the a_- mode, on the other hand, rotates against the collective spin, and

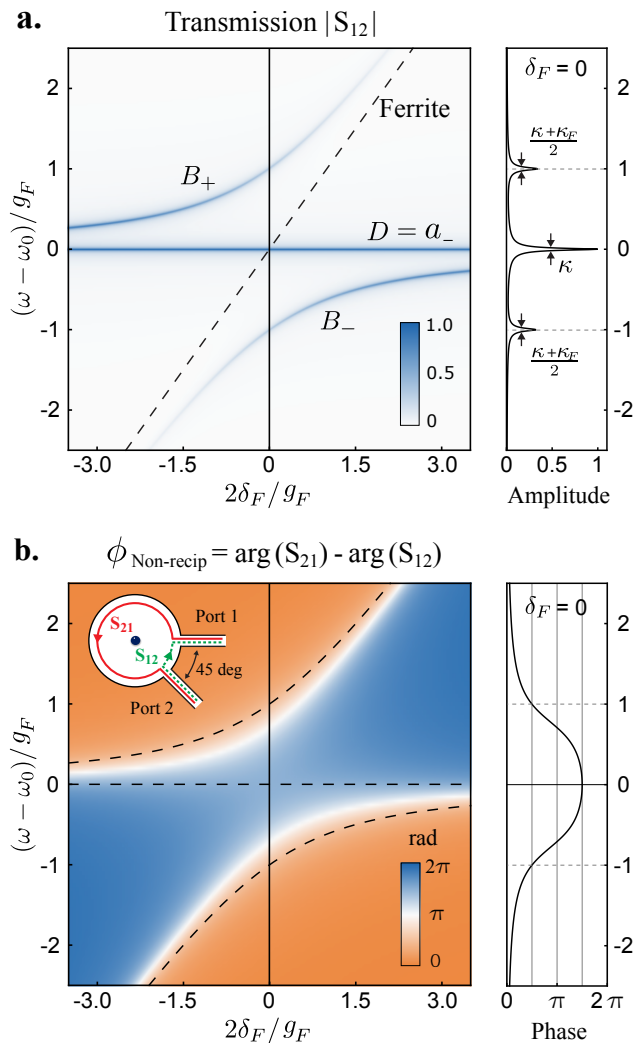


FIG. 2. Response of a ferrite-cavity site described by $\mathcal{H}^{(F)}$ in a pump-probe experiment. Here, S_{ij} is the response between a port $i = 1$ located at the \hat{x} axis, and a second port $j = 2$ measured 45 degrees away (inset to (b)). In order to account for loss, we introduce a linewidth κ and κ_F for the microwave cavity and ferrite respectively. For physically relevant values of $\kappa/g_F, \kappa_F/g_F < 10^{-2}$, this gives a corresponding cooperativity $\eta = 4g_F^2/\kappa\kappa_F > 10^4$. (a) Amplitude of the transmission response $|S_{12}|$. The chirality of a ferrite in a magnetic field allows it to couple only to the resonator mode of the same handedness, producing an avoided crossing in the transmission spectrum as the ferrite is tuned through resonance with the resonator modes. This avoided crossing appears as two modes which are bright to the ferrite, B_+ and B_- . The dark mode, labeled D , does not couple to the ferrite, and is therefore unshifted and insensitive to ferrite loss κ_F . (b) The non-reciprocal phase, $\phi_{\text{Non-Recip}} = \arg(S_{21}) - \arg(S_{12})$, reflects the phase difference between going in the 0 degree port and out the 45 degree port, and the reverse process. This is ideally $\phi_{\text{Non-Recip}} = 3\pi/2$ for the dark mode. This time-reversal break is robust to detuning in either the ferrite or the probe, and also loss, with the lowest order correction entering as $\phi_{\text{Non-Recip}} \approx \frac{3\pi}{2} - 2 \frac{\delta_P(\delta_P - 2\delta_F)}{g_F^2} - \frac{2}{\eta}$. (c) A slice through the non-reciprocal phase as a function of the probe detuning, for the ferrite tuned to resonance. The non-reciprocal phase of $\phi_{\text{Non-Recip}} \approx 3\pi/2$ is apparent near the dark mode.

thus does not couple. This results in strong hybridization of the a_+ mode with the ferrite, producing two bright magnon modes that are pushed away from the dark a_- mode at frequency ω_0 . Thus, when the system is probed near ω_0 , the isolated dark mode a_- sets a unique magnetic field polarization vector, or equivalently a unique quantum mechanical phase at the cavity periphery.

The coupling of the cavity-ferrite system is described by the Hamiltonian $\mathcal{H}^{(F)} = \mathcal{H}^{(1)} + \omega_F a_F^\dagger a_F + g_F (a_+^\dagger a_F + a_F^\dagger a_+)$, where g_F is the coupling of the ferrite to the a_+ mode (and must overwhelm Δ_{lin}). A more suggestive notation is: $\mathcal{H}^{(F)} = (\mathbf{a}^{(F)})^\dagger H^{(F)} \mathbf{a}^{(F)}$, where we have defined a ferrite-cavity mode vector $\mathbf{a}^{(F)} = (a_x, a_y, a_F)^T$ and described the cavity-ferrite system with a coupling matrix:

$$H^{(F)} = \omega_0 \hat{I} + \begin{pmatrix} 0 & 0 & g_F/\sqrt{2} \\ 0 & 0 & ig_F/\sqrt{2} \\ g_F/\sqrt{2} & -ig_F/\sqrt{2} & 2\delta_F \end{pmatrix}, \quad (1)$$

where $2\delta_F$ is the detuning of the ferrite from cavity resonance ($\omega_F = \omega_0 + 2\delta_F$) and \hat{I} is the identity matrix in the cavity-ferrite space. This Hamiltonian has an uncoupled dark eigenmode a_- that remains at frequency ω_0 . There are also two hybridized magnon modes $B_\pm = (a_F \pm a_+)/\sqrt{2}$ that are frequency shifted by $\omega_{B_\pm} - \omega_0 = \delta_F \pm \sqrt{\delta_F^2 + g_F^2}$. We henceforth assume the experimentally relevant limit where g_F is large compared to δ_F , along with any energy scales appearing in \mathcal{H}_{eff} .

Key features of this system are understood by examining the cavity response using input-output formalism [24, 30]: We consider response at a small detuning $\delta_p = \omega - \omega_0$, and ferrite detuning $2\delta_F$, from ω_0 , and introduce a finite lifetime of the cavity modes (κ) and ferrite mode (κ_F), with a resulting cooperativity $\eta = 4g_F^2/\kappa\kappa_F$. The amplitude of the response is shown in Fig. 2(a). Here, there are three maxima in the response as δ_p is varied, corresponding to three eigenmodes: the a_- mode remains at ω_0 for all ferrite detunings, while the a_+ mode mixes with the ferrite mode a_F and undergoes an avoided crossing as the ferrite detuning is swept. When probed at frequencies near ω_{B_\pm} , the bright magnon modes have the TRSB phase winding. Importantly, though only the bright mode couples to the ferrite, both the bright and dark modes are non-reciprocal. In fact the dark mode is preferred because crucially, it is insensitive to loss in the ferrite and is less sensitive to detuning and linear disorder. When the ferrite is exactly on resonance ($\delta_F = 0$), the dark mode has an exact TRSB phase winding of 2π at the periphery of the cavity. At probe frequencies different than ω_0 the phase winding ceases to be uniform. However, this nonuniformity is quadratically insensitive in both the ferrite detuning and the energy of the probe photon. This can be seen from the saddle-point structure in Fig. 2(b). Here the non-reciprocal phase response of this system is calculated between two cavity contacts separated by an angle of $\pi/4$ on the cavity periphery (inset);

the difference between forward and backwards phases is $\phi_{\text{Non-Recip}} \approx \frac{3\pi}{2} - 2\frac{\delta_p(\delta_p - 2\delta_F)}{g_F^2} - \frac{2}{\eta}$. This quadratic insensitivity of the eigenmode structure significantly decreases disorder in \mathcal{H}_{eff} arising from disorder in the ferrite, cavity, or bias field.

We now define our onsite Hamiltonian at a site j with the notation $\mathcal{H}_{\text{os},j}^{(\alpha)} = (\mathbf{a}_j^{(\alpha)})^\dagger H_j^{(\alpha)} \mathbf{a}_j^{(\alpha)}$ where $\alpha = 0$ corresponds to a fundamental cavity, $\alpha = \theta$ defines a site isolating a linear mode a_θ , and $\alpha = F$ corresponds to a ferrite site. The form of the vector of annihilation operators on site j depends on the type of site with $\mathbf{a}_j^{(0)} = a_{j0}$, $\mathbf{a}_j^{(\theta)} = (a_{jx}, a_{jy})^T$, and $\mathbf{a}_j^{(F)} = (a_{jx}, a_{jy}, a_{jF})^T$ for a fundamental, linear, and ferrite site respectively. The onsite coupling Hamiltonians are $H_j^{(0)} = \omega_0$,

$$H_j^{(\theta)} = \begin{pmatrix} \omega_0 & -\Delta_{\text{lin}} e^{i\theta} \\ -\Delta_{\text{lin}} e^{-i\theta} & \omega_0 \end{pmatrix},$$

and $H_j^{(F)}$ is given by Eq. (1). A system of uncoupled cavities is then generically described by the on-site Hamiltonian $\mathcal{H}_{\text{os}} = \sum_j \mathcal{H}_{\text{os},j}^{(\alpha)} = \sum_j (\mathbf{a}_j^{(\alpha)})^\dagger H_j^{(\alpha)} \mathbf{a}_j^{(\alpha)}$, where each α_j represents one of the distinct cavity types.

B. Tunnel coupling and nontrivial flux

Coupling of the cavities is realized by connecting their edges with evanescent waveguides. The amplitude of such a tunnel coupling is determined by the geometry (length and cross-section) of the channel. We emphasize that the coupler is only virtually populated – the evanescent wave “propagates” with a purely imaginary wavevector – so the phase of the photon is spatially uniform throughout the channel, and the channel has no dynamical degree of freedom.

Now consider a site with an isolated eigenmode (such as a_θ or a_\pm) at frequency ω_0 , that has a nonuniform phase profile. Attached to this cavity are two or more tunnel contacts to nearby cavities. The nonuniform phase of the mode implies that a photon that tunnels in along one channel will acquire a geometrical phase shift as it tunnels out along a different channel; this is the origin of the induced TRSB flux.

In a fundamental mode cavity, both the amplitude and phase around the edge are uniform, and therefore no geometric phase will be acquired for two tunneling contacts, regardless of where they are attached. In contrast, a ferrite-cavity site with two tunneling channels separated by an angle ϕ on the cavity perimeter will experience a geometrical phase shift of $\pm\phi$ for an isolated a_\pm mode (see Fig. 1(b).)

On the other hand, two tunnel contacts on a site with a mode a_θ will experience a relative phase shift only if the photon crosses a node between the processes of tunneling in and tunneling out (see Fig. 1(b).) For an a_θ mode, the local amplitude at the cavity periphery will be

nonuniform and the tunneling magnitude will gain position dependence (see Figs. 1(a).) (An ideal point contact at an angle ϕ relative to the \hat{x} axis will tunnel with amplitude $t \sim \cos(\theta - \phi)$ at frequencies near ω_0 .) This is in contrast to a mode a_0 or a_{\pm} , for which the mode magnitude, and thus the tunneling magnitude, is uniform.

For an open 1D chain of tunnel-coupled cavities, the geometric phase arising from onsite elements can be eliminated through a gauge transformation. On the other hand, closing the loop produces a net phase (flux) after tunneling around a closed loop (plaquette). This flux is analogous to a discrete version of Berry's phase and cannot be eliminated through a gauge transformation. Rather it will, appear on the tunnel coupling terms in \mathcal{H}_{eff} . In this way, a variety of lattice models can be realized that have nontrivial Peierl's phases.

C. Band projection and geometric phase

The arguments above suggest there is a nontrivial Berry's flux through a plaquette when energy scales are restricted to a small window around ω_0 (and onsite perturbations are sufficiently large). At energies away from ω_0 the full degrees of freedom must be considered. The Hamiltonian that describes this general system is given by $\mathcal{H}_0 = \mathcal{H}_T + \mathcal{H}_{\text{os}}$, where $\mathcal{H}_T = \sum_{\langle ij \rangle} \left(\mathbf{a}_i^{(\alpha_i)} \right)^\dagger T_{ij} \mathbf{a}_j^{(\alpha_j)}$ tunnel couples the lattice of cavities defined by \mathcal{H}_{os} in the previous section. The matrix T_{ij} represents the tunneling between two neighboring sites with onsite mode structure α_i and α_j . The specific form depends on the type of tunneling, but we note that an ideal point contact will have a non-zero overlap for only a single bare cavity mode (not a coupled eigenmode) at frequency ω_0 . For fundamental cavities this is naturally a_0 , whereas in first excited cavities only one linear combination of a_x and a_y will have a nonzero contribution to T_{ij} . All other tunneling terms will vanish.

The geometric flux can now be rigorously calculated considering a unitary $U_j^{(\alpha)}$ matrix at every site j that locally diagonalizes $H_j^{(\alpha)}$: $H_j^{(\alpha)} = U_j^{(\alpha)} \Delta_j^{(\alpha)} \left(U_j^{(\alpha)} \right)^\dagger$, where $\Delta_j^{(\alpha)}$ is a diagonal matrix of onsite energy eigenvalues with a unique mode at frequency ω_0 . Applying this unitary rotation to every site then transforms the Hamiltonian to $\mathcal{H}_{\text{os}} = \sum_j \left(\tilde{\mathbf{a}}_j^{(\alpha_j)} \right)^\dagger \Delta_j^{(\alpha_j)} \tilde{\mathbf{a}}_j^{(\alpha_j)}$, and $\mathcal{H}_T = \sum_{\langle ij \rangle} \left(\tilde{\mathbf{a}}_i^{(\alpha_i)} \right)^\dagger \tilde{T}_{ij} \tilde{\mathbf{a}}_j^{(\alpha_j)}$, where $\tilde{\mathbf{a}}_j^{(\alpha_j)} = U_j^{(\alpha_j)} \mathbf{a}_j^{(\alpha_j)}$ and $\tilde{T}_{ij} = U_i^{(\alpha_i)} T_{ij} \left(U_j^{(\alpha_j)} \right)^\dagger$. This transformation has the effect of locally diagonalizing each onsite Hamiltonian at the cost of transforming the tunneling matrix between sites.

The restriction to the unique mode at frequency ω_0 will amount to a projection into the onsite modes \hat{a}_{j0} . Applying a projection operator \mathcal{P}_{j0} to eliminate unoccupied

modes results in $\mathcal{H}_{\text{eff},0} \equiv \sum_j \mathcal{P}_{j0} \mathcal{H}_0 \mathcal{P}_{j0} = \sum_j \omega_0 \hat{a}_{j0}^\dagger \hat{a}_{j0} + \sum_{\langle ij \rangle} \hat{t}_{ij} \hat{a}_{i0}^\dagger \hat{a}_{j0}$, where the effective tunneling matrix \hat{t}_{ij} can contain a nontrivial phase. We emphasize that while this tunneling phase is gauge dependent, the net flux through a plaquette naturally remains gauge invariant.

We now discuss how the circuit elements described above can result in interesting band structures for a frequency range around ω_0 . For a plaquette consisting of only fundamental mode cavities, a photon acquires no net phase going around a plaquette (corresponding to zero flux.) An a_θ mode cavity would contribute a net flux of π to a plaquette if the tunneling contacts cross the nodal line, and 0 otherwise.

For plaquettes with ferrite sites, the TRSB flux is directly proportional to the angle between the two tunneling channels attached to the ferrite cavity. Thus, a resonator with N evenly spaced tunneling contacts will contribute a flux of $\phi = 2\pi/N$ to each adjacent plaquette connected by tunnel couplers. This will allow for simulation of $\alpha = 1/N$ Hofstadter models in different lattice geometries, such as $\alpha = 1/4$ in a square geometry and $\alpha = 1/6$ in a triangle. In general, using only the first excited modes we are limited to a total flux of 2π per internal ferrite. However, using higher order modes allows for a net flux of any integer multiple of 2π per plaquette.

The nontrivial effective flux is a discrete geometric (Berry's) phase; it is a direct lattice analogue to "synthetic gauge fields" studied in ultracold atomic systems [7]. There, Raman fields are used to couple internal (spin) degrees of freedom. The Raman fields vary slowly in space, but also provide a large energetic separation between dressed states. After preparing the system in a single dressed state, the dynamics respond analogously to a system under the influence of a nontrivial external gauge potential. Similar to the study of synthetic gauge fields in ultracold atoms, the microwave lattice scheme can also be extended to the regime of synthetic non-Abelian gauge fields, such as spin-orbit coupling [7, 31]; we leave such systems to future work.

D. Simulating a Hofstadter model

Given the circuit elements described above, it is now straightforward to construct an $\alpha = 1/4$ Hofstadter model. Of the many equivalent configurations, we present one that requires the minimum number of ferrites per unit cell.

Consider a square lattice of fundamental resonators, with every fourth fundamental cavity replaced by ferrite cavity, such that all plaquettes include one ferrite. This results in a square four-site unit cell. (See shaded area in Fig. 3(a).) This is consistent with the fact that a Hofstadter model with flux $\alpha = p/q$ will have a q -site unit cell. When the system is probed at frequencies near ω_0 , the time-reversal symmetry breaking mode will contribute a phase of $\pi/2$ into each of the four neighboring plaquettes. Since each plaquette touches only a single ferrite

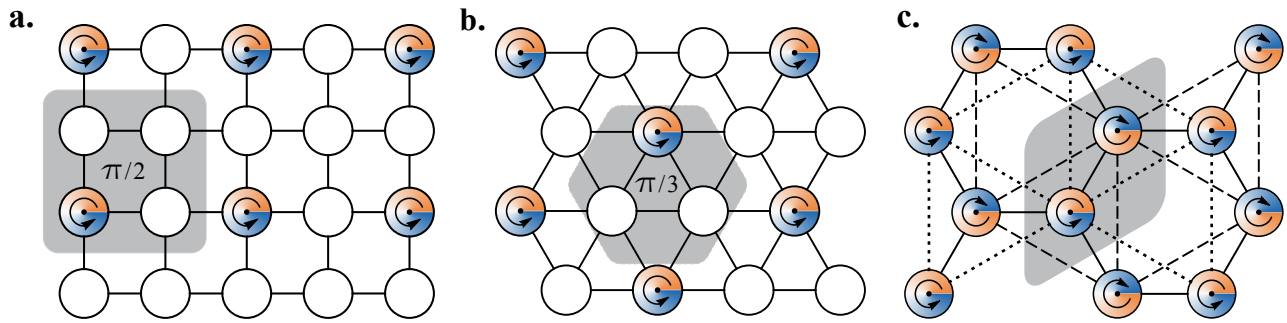


FIG. 3. Implementations of topological band structures described in the main text. (a) Hofstadter model with $\alpha = 1/4$: a square, four-site, unit cell has one ferrite and three fundamental resonators. In the effective model near a frequency ω_0 , the ferrite induces a quarter flux quantum for each of the four neighboring plaquettes. (b) Triangular Hofstadter model with $\alpha = 1/6$: a triangular lattice with a three site unit cell has a single ferrite. This ferrite touches each of six neighboring plaquettes. (c) Haldane model: a hexagonal lattice has a ferrite on each lattice site. By staggering the handedness of the dark modes on A and B sublattices, the net flux vanishes. Addition of next-nearest-neighbor tunneling terms breaks time-reversal symmetry by inducing a flux of $\alpha = \pm\pi/3$ in each sublattice.

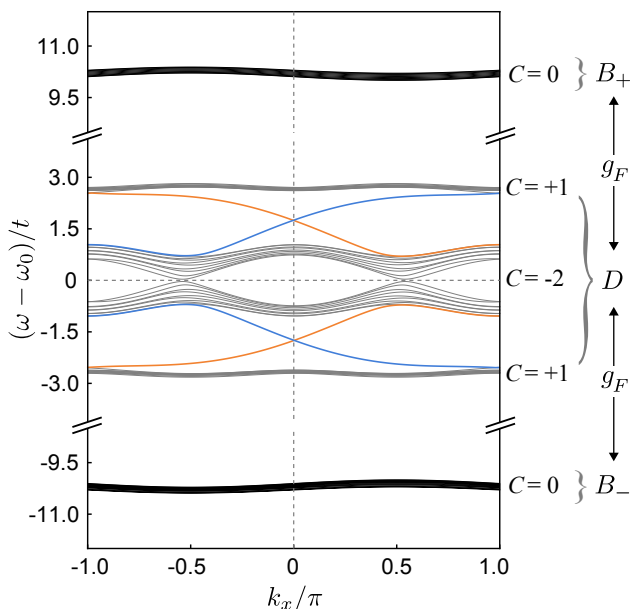


FIG. 4. Band structure of the microwave cavity implementation of the $\alpha = 1/4$ Hofstadter model in a strip geometry. The unit cell presented in Fig. 3(a) has three fundamental mode cavities, along with a single ferrite site, resulting in a total of six bands. When the ferrite energy is tuned large, two bright bands (black) are far separated from the four bands (gray) bands near ω_0 . These four bands have an edge state and Chern number structure consistent with the $\alpha = 1/4$ Hofstadter model. Here, blue (orange) lines connecting the bulk bands represent edge modes localized on the left (right) edge. No edge states connect the dark bands to the bright bands.

the total flux will be uniform $\alpha = (\pi/2)/2\pi = 1/4$.

We have verified this system provides the expected Hofstadter physics in two ways. First, we have explicitly calculated the band projected model for the phase con-

vention defined above. The net flux through a plaquette is found to be $\pi/2$ as expected. Second, we have numerically diagonalized the Hamiltonian including all relevant degrees of freedom. We chose the ferrite-cavity coupling to be ten times the tunneling energy ($g_F = 10t$), and consider a strip geometry. As seen in Fig. 4, the full model has six bands. The top and bottom (black) bands are composed almost entirely of the bright magnon modes. These bands are only weakly dispersive, as tunneling between bright modes must occur off-resonantly through neighboring fundamental cavities, and is therefore suppressed to $\sim t^2/g_F$.

In contrast, the middle four (gray) bands are composed almost entirely of dark and fundamental cavity modes. These states form the effective Hofstadter model, and have all expected properties: The four bands are energetically symmetric around the energy ω_0 ; the top and bottom band are gapped relative to the two middle bands, which touch at two distinct Dirac points; the band Chern numbers for the continuum model are calculated to be (from top to bottom) $C = 0, 1, -2, 1, 0$, consistent with topologically trivial bright bands sandwiching an $\alpha = 1/4$ Hofstadter model in the dark sector. A finite size calculation shows chiral edge channels that emerge between the Hofstadter bands, but not between the dark (Hofstadter) and bright bands.

E. Other lattice models

These circuit elements are powerful for implementing a variety of topological band structures. In passing we present two additional examples. Figure 3(b) is an implementation of a triangular Hofstadter model with $\alpha = 1/6$, where we use a triangular lattice with a single ferrite placed in each three site unit cell. Using arguments similar to above, this introduces a net flux of $\alpha = 1/6$ per plaquette, as desired.

Tunnel couplings may additionally cross by, e.g., machining channels on both the top and bottom of the substrate supporting the cavity array. This allows for implementation of an even larger class of topologically non-trivial single particle Hamiltonians. In Fig. 3(c) the Haldane model is constructed from a hexagonal lattice with next-neighbor tunnel couplings added, where a ferrite is added to every site. By alternating the sign of the DC bias field, and thereby the chirality of the ferrite dark modes, between A and B sites the net flux per plaquette vanishes, while time reversal symmetry is locally broken. This geometry specifically produces the “ideal” flux configuration that is gauge equivalent to a flux quantum per plaquette [32].

In addition to the examples presented here, other frequently studied Hamiltonians such as the 2D chiral- π [32], or 1D chiral models such as the SSH model may also be directly implemented [33]. The circuit architecture described above is useful for realization of a variety of paradigmatic lattice models described in the literature. The possibilities are extensive and we leave elucidation of these to future works.

III. EXPLORING FRACTIONAL QUANTUM HALL PHYSICS

The microwave architecture above is linear and should be equally effective at simulating non-interacting topological structures in both the classical and few-photon limits. On the other hand, to create strongly correlated topological states, strong photon-photon interactions are required. It is well established that a nonlinear interaction between photons arises through coupling the microwave cavities to Josephson junction qubits [27, 34]. The addition of a qubit to each site of the synthetic $\alpha = 1/4$ Hofstadter model proposed above should be sufficient to explore bosonic fractional-quantum hall physics [9, 28] for microwave photons. We expect that the addition of interactions should result in a FQH-like eigenstate lying at the edge of the dark bands, and well separated from the bright bands.

These FQH could then be explored in a variety of ways. For example, a pump-probe experiment with low average photon number near the energies of the effective FQH manifold. Alternatively, a chemical potential for photons [35] could be used to drive the system to a steady state with the precise number of photons requisite for a specific geometry. In finite size systems, the desired FQH eigenstates will be ones with definite photon number. We note that these preparation schemes precisely set the photon number, and thus the assumption of definite photon number below is experimentally relevant.

We now demonstrate the existence of bosonic FQH eigenstates in our architecture by numerically exploring the combined single-particle and interacting Hamiltonian $\mathcal{H}_{\text{eff,mb}} = \mathcal{H}_{\text{eff,0}} + \mathcal{H}_{\text{eff,I}}$ projected to describe

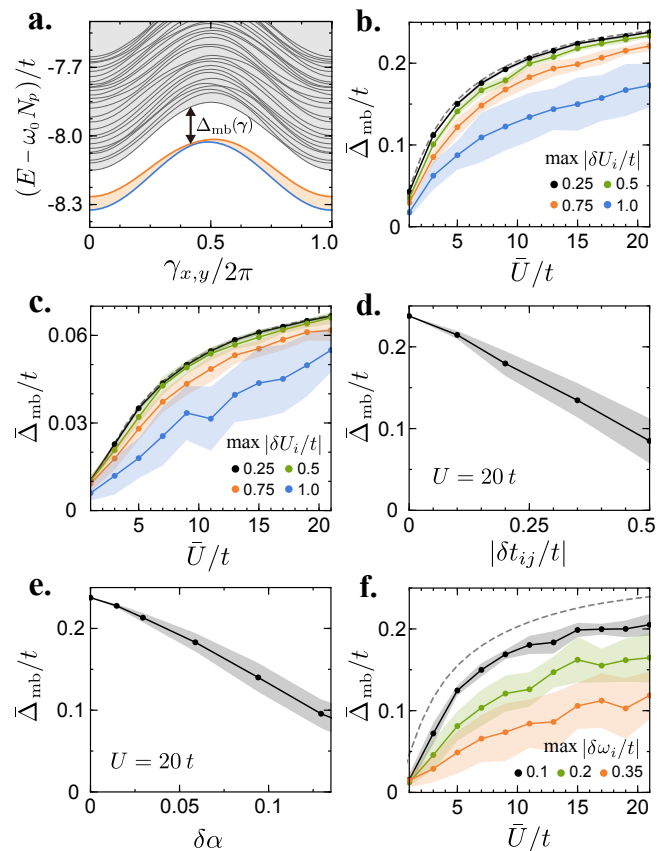


FIG. 5. (a) Spectral flow of a of the lowest 30 many-body eigenstates as a flux $\gamma_x = \gamma_y = \gamma$, $\gamma \in [0, 2\pi]$ is inserted into $\mathcal{H}_{\text{eff,mb}}$. Weak disorder is included that visually splits the numerically exact two-fold degeneracy of the ground state manifold in the clean limit. For all flux, the GSM (orange, blue lines) remains gapped relative to the (shaded gray) excited states. Provided this gap remains in the presence of disorder, a many-body Chern number can be defined. The disorder-averaged minimum value of this gap is denoted $\bar{\Delta}_{\text{mb}}$. This is used as a metric to test sensitivity to various types of disorder. (b) $\bar{\Delta}_{\text{mb}}$ as a function of the average interaction strength \bar{U} for various strengths of interaction disorder δU_i . The many-body gap is not significantly suppressed at large interaction strengths. (c) Same as (b), but all ferrite sites are made non-interacting. This comes at the cost a drop of $\bar{\Delta}_{\text{mb}}$ by a factor of about four. (d) Effect of disorder in the magnitude of the tunneling strength $|\delta t_{ij}|$, in a strongly interacting case ($U_i = 20$). (e) Effect of disorder in the flux $\delta\alpha$ through each plaquette. (f) Effect of disorder $\delta\omega_i$ in the frequency of the onsite eigenmode near ω_0 . All error bars (shaded regions) are standard errors of the mean for about 30 realizations of the disorder; the disorders δU_i , $|\delta t_{ij}|$, and $\delta\omega_i$ are uniformly distributed, whereas $\delta\alpha$ is the half-width half-max of a Gaussian distribution.

energies near ω_0 . Provided the strength of the interactions is weak compared to the ferrite-cavity coupling, a projected qubit-mediated interaction Hamiltonian can be used: $\mathcal{H}_{\text{eff,I}} = \frac{1}{2} \sum_i U_i \hat{n}_{i0} (\hat{n}_{i0} - 1)$ where U_i is the effective photon-photon interaction for the photon number

\hat{n}_{i0} of the unique mode near ω_0 at site i . We will work at a fixed particle number relevant for both numerical calculation and experiments where an exact number of photons can be prepared.

We consider a finite-size geometry with $N = N_x \times N_y$ lattice sites and toroidal boundary conditions, producing a degenerate ground state manifold. Such boundary conditions need not be a purely theoretical construct: They could be implemented explicitly by either machining the cavities on a physical torus, or connecting the opposite boundaries with waveguides [36]. In order to maintain a uniform effective flux each plaquette must touch exactly one ferrite. This geometric restriction forces $N/4$ to be an integer, and thus that the projected model has $N_\phi = \alpha N = N/4$ flux quanta. For a system of fixed particle number N_p , a FQH ground state is expected to emerge when the filling factor $\nu = N_p/N_\phi$ is expressible as a certain sequence of rational numbers. The most stable (largest many-body gap) filling is desirable; this occurs at a filling $\nu = 1/2$, which further restricts $N_p = N/8$ particles (N divisible by eight). It is experimentally advantageous to start with few photon states; we thus explore small geometries with $N_x = 4$ and $N_y = 2, 3, 4$ (and therefore $N_y = 2N_p$); all numerical results presented below are for $N_p = 3$ and $N_y = 6$. (Interestingly, this geometry produces non-dispersive bands with $N_y = 4$, which are only weakly dispersive when $N_y = 6, 8$ [37].)

As explored in previous works [3, 4, 37, 38], many properties of the FQH are expected to survive in small few-particle geometries. To demonstrate this for our system, we start by exactly diagonalizing $\mathcal{H}_{\text{eff,mb}}$ in the clean limit with $U_i = U \gg t$. The geometries described above result in a two-fold degeneracy (exact to numerical precision) in the many-body ground state manifold (GSM), as expected for a $\nu = 1/2$ Laughlin state [1, 28]. We label the states in the GSM as $|\Psi_1\rangle$ and $|\Psi_2\rangle$; translational invariance allows these states to be distinguished by their center-of-mass momentum [4]. It will be useful to impose twisted boundary condition: $\Psi_m(x + N_x, y) = e^{i\gamma_x} \Psi_m(x, y)$ and $\Psi_m(x, y + N_y) = e^{i\gamma_y} \Psi_m(x, y)$ for all eigenstates $\Psi_m(x, y)$, both in the GSM ($m = 1, 2$) and not in the GSM ($m \geq 3$). The phases $\gamma_x \times \gamma_y$ represent an Aharonov-Bohm flux $\gamma_{x,y} \in [0, 2\pi)$ adiabatically inserted along the \hat{x}, \hat{y} axes of the torus (as could be implemented with rf-modulated tunneling [19, 22].)

Figure 5(a) shows the spectral flow of the lowest 30 eigenstates as a flux quantum is simultaneously inserted along both axes of the torus. Throughout this process the GSM remains. (Here, we include disorder to visually split the two ground states; in the clean limit the GSM is degenerate to numerical accuracy for all flux values.) For each flux γ we define the spectral gap to the first set of excited states:

$$\Delta_{\text{mb}}(\gamma) = \min_{m \notin \text{GSM}} E_m(\gamma) - \max_{m \in \text{GSM}} E_m(\gamma), \quad (2)$$

and we find that the spectral gap is approximately constant for all flux $\gamma = (\gamma_x, \gamma_y) \in \text{MBZ}$, where MBZ is

the many-body Brillouin zone. Since the GSM remains gapped through the full flux insertion process, we can define the many-body Chern number [39]:

$$C_m = \frac{1}{4\pi} \int_{\gamma \in \text{MBZ}} d^2\gamma [\nabla_\gamma \times \langle \Psi_m(\gamma) | \nabla_\gamma | \Psi_m(\gamma) \rangle], \quad (3)$$

for a state $m \in \text{GSM}$. This Chern number will evaluate to an integer and give a quantized hall conductance. For a clean system, both states in the GSM can be identified by their center-of-mass momentum and C_m calculated independently. In this case we find they each carry a fractionalized many-body Chern number of $C = 1/2$, consistent with the thermodynamic limit. This result is also consistent with prior numerical studies of FQH systems, and an exact solution for a disorder-free finite-size Hofstadter model [37].

In contrast, arbitrarily weak disorder will break translational invariance and remove the degeneracy of the GSM. (This is a finite size effect, as the degeneracy remains in the thermodynamic limit.) The states in the GSM will remain gapped at all flux values. The calculation of C_m is then defined for the m -th energy level. We numerically find that with weak disorder, one state in the GSM randomly obtains $C = 1$, while the other has $C = 0$, depending on the specific disorder configuration. As the disorder strength is increased, the spectral gap may shrink until the GSM and the first excited set of states are close enough to strongly mix. In this case, the many-body Chern number may mix with the excited state manifold and destroy the FQH state. (Note that level repulsion will prevent the gap from ever exactly vanishing.) In order to quantify the tolerance to disorder, we define the minimum of the many-body gap as

$$\Delta_{\text{mb}} = \min_{\gamma \in \text{MBZ}} \Delta_{\text{mb}}(\gamma). \quad (4)$$

This quantity will be used to study the stability of our scheme in the next section.

A. Robustness to disorder

In any realistic implementation, disorder is present in various forms. We now study the influence of spatial disorder in (1) interaction strength, (2) tunneling energy, (3) flux through each plaquette, and (4) onsite energy upon the interacting Hofstadter model described above. For each disorder type we calculate the minimum many-body gap, and then average over many disorder configurations. This disorder average many-body gap, $\bar{\Delta}_{\text{mb}}$, will be used as a heuristic for the disorder tolerance of the FQH state.

We expect the FQH state to be robust to disorder in the interaction strength, provided that the average interaction strength is large compared to the tunneling energy. In this blocked limit, the two-photon wavefunction overlap is small on any given site, resulting in

only a small energy shift from interaction disorder. (This argument also applies to the continuum case where the Laughlin wavefunction has minimal overlap between photons, and therefore quenches interaction energy.) This expectation is confirmed through exact diagonalization: The stability of the many-body gap was calculated by taking the smallest gap as a full 2π flux was inserted through the twisted boundary conditions, as in Eq. (4). This calculation was performed for a range of average interaction strengths up to $\bar{U}_i \sim 20t$, with a disorder strength $\delta U_i = U_i - \bar{U}$ uniformly distributed in the different ranges of $\pm\bar{U} \times \{\frac{1}{4}, \frac{1}{2}, \frac{3}{4}, 1\}$. The results are shown in Fig. 5(b) demonstrating that interaction disorder does not significantly reduce the many-body gap. We further numerically verified that for all disorder configurations the many-body gap remained open throughout flux insertion, and the total many-body Chern number in the ground state manifold remained $C = 1$.

It is curious that even for the case of the strongest interaction disorder ($\max_i |\delta U_i| = \bar{U}$) when certain lattice sites can be almost non-interacting, the topological state survives with a many-body gap that does not seem to be limited by the smallest U_i in the system. In our system, we still expect only a small probability for the overlap of two photons, and therefore a robustness to completely removing some number of qubits. Removing qubits may provide additional flexibility to the proposed experimental realization of the interacting lattice, as the ferrites require a large bias DC magnetic field that is detrimental to the operation of superconducting qubits. We therefore repeat the previous calculation, now with interactions turned off entirely on all ferrite sites (see Fig. 5(c)). We find the topological ground state is preserved, although the disorder-averaged many-body gap $\bar{\Delta}_{\text{mb}}$ is reduced by a factor of ~ 4 .

For interaction disorder we considered a wide distribution which will realistically arise due to fabrication variations in qubits. By contrast, tunneling disorder will be small due to a combination of precision machining techniques and the quadratic insensitivity of the dark state on ferrite sites. We still consider small to moderate disorder in both amplitude ($|\delta t_{ij}|$, uniformly distributed) and phase of the tunneling rates; the disorder in phase translates to a (Gaussian distribution) disordered flux in each plaquette of $\delta\alpha$. The resulting many-body gaps are plotted in Fig. 5(d)-(e) when the photon-photon interactions are assumed to be large. We find the many-body gap decreases only linearly for both tunneling disorder types in this regime, suggesting that tunneling disorder will not be a significant issue in experiment.

The system is more sensitive to onsite disorder which shifts the onsite mode frequency to $\omega_0 \rightarrow \omega_0 + \delta\omega_i$. We explore this physics in Fig. 5(f) by adding random onsite (uniformly distributed) disorder in the exact diagonalization calculation. The situation is similar to previous results for disordered (fermionic) FQH systems [40, 41]: The total many-body Chern number of the ground state manifold is probabilistically distributed between the low-

est lying states for small disorder. At larger disorder a collapse of a mobility gap results in a transition to an insulating state. We find that for weak disorder, the many-body gap persists, but declines roughly linearly in the disorder strength. Using 3D microwave cavities, onsite disorder is given by variations in the cavity resonances determined by the cavity dimensions and can precisely controlled with modern machining techniques. Additionally, the onsite resonance can be made tunable, over a range larger than the tunneling t , by e.g. using a tuning screw or piezo stack to perturb critical dimensions of the cavity [42]. Combined with tomography techniques [43, 44] which can map out a tight-binding Hamiltonian, onsite disorder can be characterized in the fully coupled lattice, and further reduced.

IV. DISCUSSION

We have presented a scalable 3D microwave circuit architecture to explore bosonic FQH models of photons. Central to this approach is a method for implementing the necessary TRSB flux of the single particle band structure: the onsite mode structure is used to induce this flux, rather than the tunnel couplers themselves. Specifically, a ferrite is used to couple a degenerate cavity manifold, resulting in an isolated cavity eigenmode at frequency ω_0 that has uniform phase winding around the cavity periphery. As a photon tunnels in and out, it will accumulate the phase difference between the input and output tunnel contact. This phase is a geometric (Berry's) phase, and will contribute a nontrivial flux to any connected plaquette. This allows for exploration of, e.g., an $\alpha = 1/4$ Hofstadter model on a square lattice. The circuit elements are entirely passive, providing a distinct advantage from competing protocols that require driving of the tunnel matrix elements.

In practice, 10GHz microwave resonators may be realized with ferrite-time reversal breaking of order $g_F = 400$ MHz [45]; this allows a Hofstadter model bandwidth of 200 MHz for tunneling energy of $J = 50$ MHz, resonator-to-resonator disorder of order ~ 1 MHz, and resonator linewidths of $\kappa \sim 20$ Hz for superconducting coaxial resonators [20], and $\kappa \sim 10$ kHz in modest magnetic fields. For standard transmon qubits, $U = 350$ MHz is readily achieved [46], providing a many-body gap of order (see above) of $\Delta_{\text{mb}} \sim 8$ MHz, which is easily resolvable. Such states may be spectroscopically populated [47], and their average occupation of $1/8$ per site verified by site-resolved spectroscopy [17].

This lattice architecture then forms the basis for the investigation of topological many-body physics. Effective photon-photon interactions are implemented through the addition of superconducting qubits. Consistent with previous works, we predict the emergence of a $\nu = 1/2$ bosonic FQH eigenstate, even at a large flux per plaquette of $\alpha = 1/4$. We further verify that this phase is relatively robust to experimentally realistic disorder in

onsite energy, interactions, tunneling energy, and flux in a plaquette. In conjunction with state of the art proposals to implement chemical potentials for photons [35, 48] this work provides a complete roadmap to photonic fractional quantum hall physics, and a path to spectroscopic creation and manipulation of anyons [49, 50].

V. ACKNOWLEDGEMENTS

This work was supported by ARO grant W911NF-15-1-0397; D.S. acknowledges support from the David and Lucile Packard Foundation; B.M.A. and R.M. acknowledge support from the UChicago MRSEC grant NSF-DMR-MRSEC 1420709; C.O. is supported by the NSF GRFP. The authors thank D. Angelakis, W. DeGottardi, M. Hafezi, and M. Levin, for helpful discussions.

-
- [1] H. L. Stormer, D. C. Tsui, and A. C. Gossard, *Rev. Mod. Phys.* **71**, S298 (1999).
- [2] A. Stern, *Annals of Physics* **323**, 204 (2008), january Special Issue 2008.
- [3] E. J. Bergholtz and Z. Liu, *International Journal of Modern Physics B*, *International Journal of Modern Physics B* **27**, 1330017 (2013).
- [4] N. Regnault and B. A. Bernevig, *Phys. Rev. X* **1**, 021014 (2011).
- [5] M. Aidelsburger, M. Atala, M. Lohse, J. T. Barreiro, B. Paredes, and I. Bloch, *Phys. Rev. Lett.* **111**, 185301 (2013).
- [6] H. Miyake, G. A. Siviloglou, C. J. Kennedy, W. C. Burton, and W. Ketterle, *Phys. Rev. Lett.* **111**, 185302 (2013).
- [7] N. Goldman, G. Juzeliūnas, P. Öhberg, and I. B. Spielman, *Reports on Progress in Physics* **77**, 126401 (2014).
- [8] G. Jotzu, M. Messer, R. Desbuquois, M. Lebrat, T. Uehlinger, D. Greif, and T. Esslinger, *Nature* **515**, 237 (2014).
- [9] N. Cooper, *Advances in Physics* **57**, 539 (2008).
- [10] M. Greiner, O. Mandel, T. Esslinger, T. W. Hansch, and I. Bloch, *Nature* **415**, 39 (2002).
- [11] I. Bloch, J. Dalibard, and W. Zwerger, *Rev. Mod. Phys.* **80**, 885 (2008).
- [12] J. Ningyuan, C. Owens, A. Sommer, D. Schuster, and J. Simon, *Phys. Rev. X* **5**, 021031 (2015).
- [13] Z. Wang, Y. Chong, J. D. Joannopoulos, and M. Soljacic, *Nature* **461**, 772 (2009).
- [14] M. C. Rechtsman, J. M. Zeuner, Y. Plotnik, Y. Lumer, D. Podolsky, F. Dreisow, S. Nolte, M. Segev, and A. Szameit, *Nature* **496**, 196 (2013).
- [15] HafeziM., MittalS., FanJ., MigdallA., and T. M., *Nat Photon* **7**, 1001 (2013).
- [16] P. J. J. O'Malley, R. Babbush, I. D. Kivlichan, J. Romero, J. R. McClean, R. Barends, J. Kelly, P. Roushan, A. Tranter, N. Ding, B. Campbell, Y. Chen, Z. Chen, B. Chiaro, A. Dunsworth, A. G. Fowler, E. Jeffrey, A. Megrant, J. Y. Mutus, C. Neill, C. Quintana, D. Sank, A. Vainsencher, J. Wenner, T. C. White, P. V. Coveney, P. J. Love, H. Neven, A. Aspuru-Guzik, and J. M. Martinis, ArXiv e-prints (2015), [arXiv:1512.06860](https://arxiv.org/abs/1512.06860) [quant-ph].
- [17] A. A. Houck, H. E. Tureci, and J. Koch, *Nat Phys* **8**, 292 (2012).
- [18] J. Koch, A. A. Houck, K. L. Hur, and S. M. Girvin, *Phys. Rev. A* **82**, 043811 (2010).
- [19] K. Fang, Z. Yu, and S. Fan, *Nat Photon* **6**, 782 (2012).
- [20] M. Reagor, H. Paik, G. Catelani, L. Sun, C. Axline, E. Holland, I. M. Pop, N. A. Masluk, T. Brecht, L. Frunzio, M. H. Devoret, L. Glazman, and R. J. Schoelkopf, *Applied Physics Letters* **102** (2013), [dx.doi.org/10.1063/1.4807015](https://doi.org/10.1063/1.4807015).
- [21] J. Cho, D. G. Angelakis, and S. Bose, *Phys. Rev. Lett.* **101**, 246809 (2008).
- [22] L. D. Tzuang, K. Fang, P. Nussenzveig, S. Fan, and M. Lipson, *Nat Photon* **8**, 701 (2014).
- [23] J. C. Maxwell, *Philosophical Transactions of the Royal Society of London* **155**, 459 (1865).
- [24] Y. Tabuchi, S. Ishino, A. Noguchi, T. Ishikawa, R. Yamazaki, K. Usami, and Y. Nakamura, ArXiv e-prints (2015), [arXiv:1508.05290](https://arxiv.org/abs/1508.05290) [quant-ph].
- [25] M. Goryachev, W. G. Farr, D. L. Creedon, Y. Fan, M. Kostylev, and M. E. Tobar, *Phys. Rev. Applied* **2**, 054002 (2014).
- [26] K. Le Hur, L. Henriët, A. Petrescu, K. Plekhanov, G. Roux, and M. Schiró, ArXiv e-prints (2015), [arXiv:1505.00167](https://arxiv.org/abs/1505.00167) [cond-mat.mes-hall].
- [27] M. Reagor, W. Pfaff, C. Axline, R. W. Heeres, N. Ofek, K. Sliwa, E. Holland, C. Wang, J. Blumoff, K. Chou, M. J. Hatridge, L. Frunzio, M. H. Devoret, L. Jiang, and R. J. Schoelkopf, ArXiv e-prints (2015), [arXiv:1508.05882](https://arxiv.org/abs/1508.05882) [quant-ph].
- [28] M. Hafezi, A. S. Sørensen, E. Demler, and M. D. Lukin, *Phys. Rev. A* **76**, 023613 (2007).
- [29] D. Pozar, *Microwave Engineering, 4th Edition* (Wiley, 2011).
- [30] M. Scully and M. Zubairy, *Quantum Optics* (Cambridge University Press, 1997).
- [31] J. Ruseckas, G. Juzeliūnas, P. Öhberg, and M. Fleischhauer, *Phys. Rev. Lett.* **95**, 010404 (2005).
- [32] T. Neupert, L. Santos, C. Chamon, and C. Mudry, *Phys. Rev. Lett.* **106**, 236804 (2011).
- [33] W. P. Su, J. R. Schrieffer, and A. J. Heeger, *Phys. Rev. Lett.* **42**, 1698 (1979).
- [34] A. Wallraff, D. I. Schuster, A. Blais, L. Frunzio, R. S. Huang, J. Majer, S. Kumar, S. M. Girvin, and R. J. Schoelkopf, *Nature* **431**, 162 (2004).
- [35] M. Hafezi, P. Adhikari, and J. Taylor, *Physical Review B* **92**, 174305 (2015).
- [36] J. Ningyuan, C. Owens, A. Sommer, D. Schuster, and J. Simon, *Physical Review X* **5**, 021031 (2015).
- [37] T. Scaffidi and S. H. Simon, *Phys. Rev. B* **90**, 115132 (2014).
- [38] E. Kapit, P. Ginsparg, and E. Mueller, *Phys. Rev. Lett.* **108**, 066802 (2012).

- [39] Q. Niu, D. J. Thouless, and Y.-S. Wu, *Phys. Rev. B* **31**, 3372 (1985).
- [40] D. N. Sheng, X. Wan, E. H. Rezayi, K. Yang, R. N. Bhatt, and F. D. M. Haldane, *Phys. Rev. Lett.* **90**, 256802 (2003).
- [41] X. Wan, D. N. Sheng, E. H. Rezayi, K. Yang, R. N. Bhatt, and F. D. M. Haldane, *Phys. Rev. B* **72**, 075325 (2005).
- [42] G. Matthaei, L. Young, and E. Jones, *Microwave filters, impedance-matching networks, and coupling structures*, Artech House microwave library No. v. 1 (McGraw-Hill, 1964).
- [43] D. Burgarth, K. Maruyama, and F. Nori, *New Journal of Physics* **13**, 013019 (2011).
- [44] R. Ma, J. C. Owens, A. LaChapelle, J. Simon, and D. Schuster, "Hamiltonian tomography of photonic lattices," In Preparation.
- [45] N. Kostylev, M. Goryachev, and M. E. Tobar, *Applied Physics Letters* **108**, 062402 (2016), [dx.doi.org/10.1063/1.4941730](https://doi.org/10.1063/1.4941730).
- [46] H. Paik, D. I. Schuster, L. S. Bishop, G. Kirchmair, G. Catelani, A. P. Sears, B. R. Johnson, M. J. Reagor, L. Frunzio, L. I. Glazman, S. M. Girvin, M. H. Devoret, and R. J. Schoelkopf, *Phys. Rev. Lett.* **107**, 240501 (2011).
- [47] P. Schausz, M. Cheneau, M. Endres, T. Fukuhara, S. Hild, A. Omran, T. Pohl, C. Gross, S. Kuhr, and I. Bloch, *Nature* **491**, 87 (2012).
- [48] M. Hafezi, M. D. Lukin, and J. M. Taylor, *New Journal of Physics* **15**, 063001 (2013).
- [49] B. Paredes, P. Fedichev, J. I. Cirac, and P. Zoller, *Phys. Rev. Lett.* **87**, 010402 (2001).
- [50] R. Umucalilar and I. Carusotto, *Physics Letters A* **377**, 2074 (2013).